

## STAR FORMATION IN THE HIGH-EXTINCTION PLANCK COLD CLUMP PGCC G120.69+2.66

ANLAUG AMANDA DJUPVIK

Nordic Optical Telescope, Rambla José Ana Fernández Pérez 7, ES-38711 Breña Baja, Spain and  
Department of Physics and Astronomy, Aarhus University, Munkegade 120, DK-8000 Aarhus C, Denmark

JOÃO L. YUN

Instituto de Astrofísica e Ciências do Espaço (IA), Universidade de Lisboa  
Departamento de Física, Faculdade de Ciências, Campo Grande, PT-1749-016 Lisboa, Portugal and  
Visiting astronomer, Departament de Física Quàntica i Astrofísica, Institut de Ciències del Cosmos, Universitat de Barcelona  
(ICC-UB), Martí i Franquès 1, E-08028 Barcelona, Spain

FERNANDO COMERÓN

European Southern Observatory, Karl-Schwarzschild-Str. 2, 85748 Garching bei München, Germany  
Version November 7, 2024

### Abstract

We investigate the star formation occurring in the Planck Galactic cold clump PGCC 120.69+2.66. Near-infrared JHK<sub>S</sub> images and K-band spectroscopy obtained with NOTCam at the Nordic Optical Telescope complemented with archive data are used to study the stellar content. In addition, millimetre line CO and CS spectra were obtained with the Onsala 20 m telescope, and sub-millimetre continuum SCUBA-2 archive data are used to characterise the host molecular cloud. We identify a molecular cloud core traced by CO and CS emission at a distance of 1.1 kpc. In the region studied, we identify 5 submm continuum cores. Embedded in and around these dense submm cores, we find 38 young stellar objects, classified as 9 Class I, 8 Class II, and 21 near-IR excess or variability sources, accompanied by bipolar nebulosities and signs of protostellar jets. Furthermore, a very bright and reddened source is found towards this molecular cloud core. Even though its location appears to suggest its association to the star formation region, its infrared spectral type is compatible with a red supergiant, hidden behind 36 mag of visual extinction.

### 1. INTRODUCTION

Detecting and classifying the young stellar population in molecular clouds at an early star formation phase is vital for the understanding of star formation process - the young stellar objects (YSOs) are the end products and the molecular cloud cores are the initial conditions in which they form. Stars tend to form in groups, often in rich clusters with hundreds to thousands of stars, but also in looser aggregates with fewer young stellar objects (Strom et al. 1993).

The presence of embedded jets and of extended nebular emission often reveals the young stellar character of the associated sources (e.g., McCaughrean et al. 1994; Yun et al. 1997, 2001). Recent large scale studies of nearby star formation regions with infrared surveys (e.g. Evans et al. 2009; Gutermuth et al. 2009; Winston et al. 2020, and references therein) have investigated large populations of embedded YSOs in their early evolutionary phases at high sensitivity and spatial resolution, locating their birthplace to the densest molecular cloud cores, often found distributed along filaments as traced by submm surveys (André et al. 2014).

Low-mass YSOs are commonly classified following their evolutionary stages (Adams et al. 1987; André et al.

1993) *i*) as Class 0 (protostars heavily embedded in their parent molecular cloud cores only seen in the submm wavelengths); *ii*) as Class I (infrared protostars surrounded by accreting envelopes and circumstellar discs); *iii*) as Class II (optical visible sources displaying near-infrared excesses due to the presence of their circumstellar discs); and finally *iv*) as transitional objects, pre-main-sequence stars close to reaching the main-sequence.

Based on previous investigations of star formation in the outer Galaxy, selecting IRAS sources with colours and temperature maps strongly correlated with the presence of embedded infrared protostars or young clusters (e.g. Yun et al. 2001; Palmeirim & Yun 2010; Yun et al. 2015), we found that the region around the IRAS source IRAS 00267+6511 was a promising candidate for an active star formation site towards the outer Galaxy ( $l = 120.7^\circ$ ,  $b = 2.7^\circ$ ). The region has been identified as a dense cloud core via CO, HCO<sup>+</sup>, and HCN emission (Zhang et al. 2016; Yuan et al. 2016) and is listed in the Planck catalog of Galactic Cold Clumps (Planck Collaboration et al. 2016) derived from three high-frequency bands (353, 545, and 857 GHz). The stellar content had not been studied, given that at optical wavelengths the region is a patch of obscuration against background stars

with no sign of star formation. Candidate YSOs had been proposed around IRAS 00267+6511 via application of automatic algorithms (e.g. Wilson et al. (2023) use a naive Bayes classifier for identifying candidate Class II YSOs in the GAIA DR3, or via vector machine selection of WISE sources (e.g. Marton et al. 2016)). Here, we seek to determine the YSO population down to fainter magnitudes and with better angular resolution than presently available for this region.

Molecular cloud cores are known to exhibit very high values of visual extinction hiding from optical view both YSOs forming in the cores and other background objects, as well. In fact, in the 2MASS (Skrutskie et al. 2006) near-IR images of the region, we became aware of an intriguingly bright and red object that caught our attention; invisible in optical surveys and situated only  $34''$  from the IRAS source, i.e. close to the center of the cloud, it could be a very bright YSO or instead a background unrelated source.

We obtained high-resolution near-infrared JHK<sub>S</sub> images and K-band spectroscopy with the Nordic Optical Telescope (Djupvik & Andersen 2010) to identify and characterise young stellar sources. In addition, we use millimetre and sub-millimetre data, both new and archive data, to define the molecular and dust environment. We report here evidence for early star formation activity in the form of nebular emission, mid- and near-infrared excess sources in the protostellar and pre-main sequence phase. The bright red source appears to be a previously unknown background massive supergiant star hidden behind several tens of magnitudes of visual extinction. Section 2 describes the observations and data reduction, in Sects. 3 and 4 we present and discuss the results, and a summary is given in Sect. 5.

## 2. OBSERVATIONS

### 2.1. Near-infrared observations

Near-IR imaging and spectroscopy was obtained with NOTCam, the Nordic Optical Telescope’s near-IR Camera and Spectrograph<sup>1</sup> The NOTCam detector is a Hawaii 1k HgCdTe IR array and the camera optics has two different scales (Abbott et al. 2000). The wide-field (WF) camera has pixel size of  $0'.234$  and a  $4' \times 4'$  field-of-view, and the high-resolution (HR) camera has a pixel size of  $0'.079$  and a fov of about  $80'' \times 80''$ .

NOTCam broad-band JHK<sub>S</sub> imaging and narrow-band imaging on and off the H<sub>2</sub> v=1-0 S(1) line at  $2.122 \mu\text{m}$ , using filters #218 and #230, were obtained in free slots in service nights with starting dates 2023-11-23, 2023-12-28 and 2024-07-17. For the K<sub>S</sub> band we used a 6 mm cold stop to avoid saturation on the bright star. (Since NOTCam is equipped with cold stops of different diameters, we could reduce the 15 mm beam inside the instrument, effectively reducing the telescope size and lowering the transmission to 15%.) The total on-source exposure times used with the WF camera were 180s (J), 194s (H), 32s (K<sub>S</sub> + 6mm stop), and 2300s (#218 and #230). Two smaller fields mapped with the HR-camera, one to the North (N) and one to the North-West (NW) of the near-IR luminous star, avoiding the bright source,

and the total on-source exposure times were 540s in each filter J, H, and K<sub>S</sub> for both of these fields. The seeing measured in these images have PSF fwhm of  $0.4''$  and  $0.6''$  for the N and the NW fields, respectively.

Differential twilight flats were obtained for all filters and domeflats for the combination of K-band and the 6mm stop. Deeper images were obtained with the HR-camera in the JHKs filters in smaller regions near the bright source. The imaging was obtained with small-step dithers, using ramp-sampling readout and individual exposure times short enough to avoid saturation. The images were reduced with IRAF<sup>2</sup> and the IRAF package notcam.cl v2.6, made for NOTCam image reductions, including bad-pixel correction, flat-field correction, sky evaluation and subtraction, distortion correction, shifting and combination the individual frames.

For each field and filter point sources are detected and measured with aperture photometry, using the IRAF photometry package, applying aperture corrections found using curve of growth on a few bright and isolated stars in each image. We cross-correlated each field with 2MASS sources with quality flag AAA, used to calibrate the NOTCam JHK<sub>S</sub> photometry, as well as the astrometry. The positional rms values are  $0.05''$  and  $0.02''$  for the WF camera and the HR-camera, respectively. The photometric calibration errors of 0.021, 0.027, and 0.054 mag for J, H, and K<sub>S</sub>, respectively, were added in quadrature to the photometric errors obtained in the WF field. For the small HR fields, calibration sources were limited to a few stars only. In the two small fields observed on different nights, there is a star that differ by less than 0.04 mag in the H and K<sub>S</sub> bands and by 0.12 in J, the latter most likely due to the faintness in the J-band (18 mag), and we decided to apply 0.04 mag as calibration error for the photometry in the HR fields.

The spectroscopy was done with the NOTCam echelle grism Gr#1, the K-band filter (#208) used as an order sorter, and the  $128 \mu\text{m}$  wide slit (corresponding to  $0.6''$  or 2.6 pixels). This setup covers the range from  $1.95$  to  $2.37 \mu\text{m}$  with a dispersion of  $4.1 \text{ \AA}/\text{pix}$ , giving a spectral resolution  $\lambda/\Delta\lambda$  of about 2100. K-band spectroscopy of the bright source was obtained on 2023-11-08, dithering along two positions on the slit (A-B) three times to obtain 6 individual spectra, each with an exposure time of 20 seconds (reading out every 4 seconds 5 times in ramp-sampling mode). Calibration lamps were taken while pointing to target to minimize flexure in the wavelength calibration and improve fringe corrections with the spectroscopic flats. To correct the spectrum for Earth’s atmospheric features we used as a telluric standard the star HD5071 (SpT B8,  $K_{2\text{MASS}} = 7.49$  mag), observed right after the target. Hot-pixel masks were constructed from darks taken with the same integration time and readout mode. For the target and the standard the individual ABABAB exposures were corrected for hot pixels, flat-field corrected using halogen flats, and sky-subtracted using the neighbouring frame. The individual 1D spectra were optimally extracted and wavelength calibrated using dedicated scripts based on IRAF tasks, after which they were combined to a final spectrum. The target spectrum was divided by the telluric spectrum using the inter-

<sup>1</sup> NOTCam is documented in detail at <https://www.not.iac.es/instruments/notcam/>.

<sup>2</sup> IRAF is currently supported and maintained by an IRAF community at <https://iraf.net/>.

active IRAF task *telluric*, having first interpolated over the stellar Br $\gamma$  absorption line at  $2.166 \mu\text{m}$  in the telluric. Differential photometry of the telluric in the acquisition image, using three reliable 2MASS stars, gave  $K = 7.56 \pm 0.02$  mag, differing by 0.07 mag from the published 2MASS value. This calibration is used to flux-scale a Vega continuum which was multiplied with the target spectrum to correct the slope and give a rough estimate of the target flux.

## 2.2. CO and CS mm line observations

Millimetre single-dish observations of IRAS 00267+6511 were carried out at the 20 m Onsala telescope, in 2009 April. Three maps were obtained in the rotational lines of  $^{12}\text{CO}(1-0)$  (115.271 GHz),  $^{13}\text{CO}(1-0)$  (110.201 GHz), and CS(2-1) (97.981 GHz), respectively. The telescope half-power beam width (HPBW) was  $32''$  at 115 GHz and  $38''$  at 98 GHz. The adopted grid spacing was  $30''$  (approximately full-beam sampling, adopted due to the limited observing time available). The  $^{12}\text{CO}(1-0)$ ,  $^{13}\text{CO}(1-0)$ , and CS(2-1) maps are composed of  $5 \times 5$ , of  $7 \times 7$ , and of  $5 \times 6$  pointings, respectively.

A high-resolution 1600 channel spectrometer was used as a back end, with a total bandwidth of 40 MHz and a channel width of 25 kHz, corresponding to approximately  $0.065 - 0.075 \text{ km s}^{-1}$ , at those frequencies. The spectra were taken in frequency-switching mode, recommended to save observational time when mapping extended sources. The antenna temperature was calibrated with the standard chopper wheel method. Pointing was checked regularly towards known circumstellar SiO masers; pointing accuracy was estimated to be better than  $4''$ .

Data reduction followed standard steps: *i*) folding the frequency-switched spectrum; *ii*) fitting the baseline by a polynomial and subtracting it; *iii*) coadding repeated spectra obtained at the same sky position; *iv*) obtaining the main beam temperature  $T_{\text{MB}}$  by dividing the antenna temperature  $T_{\text{A}}$  by the  $\eta_{\text{MB}}$  factor, equal to about 0.5 for these lines; and *v*) finally, smoothing the spectra to a velocity resolution of approximately  $0.13 - 0.15 \text{ km s}^{-1}$  at those frequencies. The spectrum baseline RMS noise (in  $T_{\text{MB}}$ ), averaged over all map positions, has been found to be 1.4 K for  $^{12}\text{CO}(1-0)$ , 0.4 K for  $^{13}\text{CO}(1-0)$ , and 0.2 K for CS(2-1).

## 2.3. Archive data

This region was surveyed by the Herschel satellite whose database is accessible via the NASA/IPAC Infrared Science Archive (IRSA). It was also observed by the Planck satellite. In this region, the *Planck Early Release Compact Source Catalogue* (Planck Collaboration et al. 2011) lists a submm clump named PLCKECC G120.67+2.66. This catalog was later superseded by the *Planck Catalogue of Galactic Cold Clumps* (Planck Collaboration et al. 2016) containing the source PGCC G120.69+2.66 (with slightly different coordinates). This clump extends by  $11'.6 \times 4'.4$  on the sky. The centre is positioned about 2 arcmin southeast of IRAS 00267+6511, and involves the whole region imaged in this study.

This region was covered by the SCUBA-2 Continuum

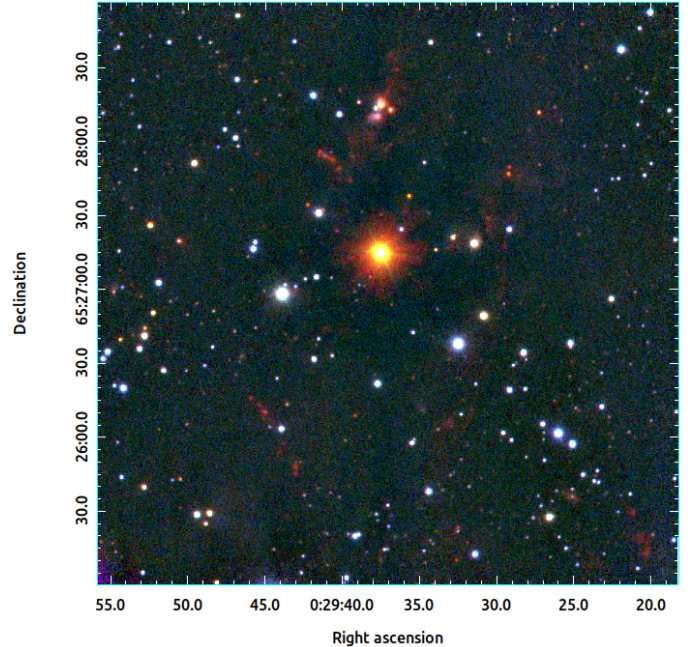


FIG. 1.— NOTCam RGB image of the Planck cold clump PGCC G120.69+2.66 region using J-band (blue), H-band (green) and  $2.122 \mu\text{m}$  H $_2$  line (red). The bright, red star near the centre is discussed in Sect. 4.4.

Observations of Pre-protostellar Evolution Large Program (SCOPE) survey (Liu et al. 2018; Eden et al. 2019). The survey was conducted at  $850 \mu\text{m}$  with a beam size of 14.4 arcsec on the James Clerk Maxwell Telescope equipped with the SCUBA-2 instrument (Holland et al. 2013). We accessed the data base via the Canadian Astronomy Data Centre and downloaded the corresponding FITS image of this region. With a pixel scale of  $4'' \text{ pix}^{-1}$ , it covers about  $10' \times 10'$  encompassing the region mapped by NOTCam and the CO and CS observations.

## 3. RESULTS

### 3.1. The mid-infrared view

We have explored the WISE (Wright et al. 2010) and 2MASS (Skrutskie et al. 2006) catalogues in the  $4' \times 4'$  region around IRAS 00267+6511 shown in the NOTCam image in Fig. 1. After weeding out extragalactic contaminants and low S/N sources in the WISE sample, we search for Young Stellar Objects (YSOs) among the sources based on their mid-IR Spectral Energy Distributions (SEDs). The standard classification scheme for YSOs is based on the shape of the mid-IR SED quantified by the SED index  $\alpha = d \log \lambda f_{\lambda} / d \log \lambda$  originally taken from 2 to 10 (or 25)  $\mu\text{m}$  (Lada & Wilking 1984; Greene et al. 1994). A steeply rising SED towards longer wavelengths for protostars embedded in dust envelopes, Class I sources ( $\alpha > 0.3$ ), can be easily separated from a declining slope of the more evolved Class II sources ( $-1.6 < \alpha \leq -0.3$ ) surrounded by circumstellar dust disks. An intermediate range would be occupied by the so-called Flat-Spectrum sources ( $-0.3 < \alpha \leq 0.3$ ). The SED index is frequently translated to colour indices in various magnitude systems that will define IR excess emission above the Rayleigh-Jeans tail of the photospheric black-body. For the WISE photometry in the bands W1 ( $3.4 \mu\text{m}$ ), W2 ( $4.6 \mu\text{m}$ ) and W3 ( $11.8 \mu\text{m}$ ) we

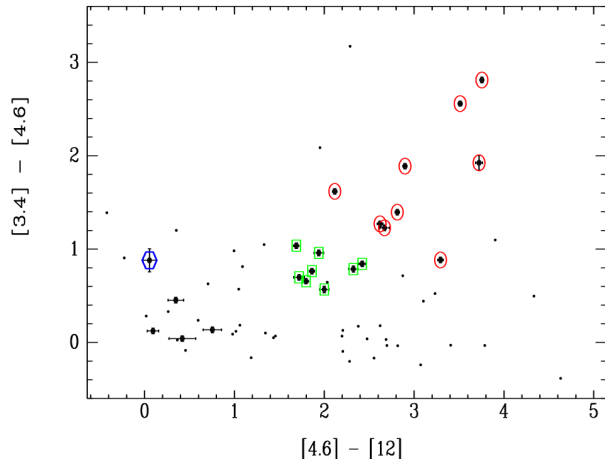


FIG. 2.— WISE  $[3.4]-[4.6]/[4.6]-[12]$  colour-colour diagramme of all 68 sources in the  $4' \times 4'$  FOV. The 22 sources with quality flag A in all the three filters are shown as larger dots with error bars. The classified Class I sources (red circles) and the Class II sources (green squares) are shown. The blue hexagon marks the position of the brightest near-IR source in the region, a candidate red supergiant, see Sect. 4.4.

apply the criteria described by Koenig & Leisawitz (2014) for removing extragalactic contaminants as well as defining the Class I and Class II sources according to their location in the  $[3.4] - [4.6]/[4.6] - [12]$  colour-colour diagramme. Following their criteria we discard 75% of the sources in the field as having no mid-IR excess. These are stars, extragalactic sources, or low S/N detections. Only 22 of the 68 sources have photometric quality flag A in all three filters. We find 17 YSOs with mid-IR excess and classify them as Class I and Class II sources as shown in Fig. 2, where the 9 Class I sources are marked with red circles while the 8 Class IIs are marked with green squares. For comparison, in the same region an all-sky study by Marton et al. (2016), using a statistical method on the WISE and 2MASS catalogues, finds 3 of the 9 Class Is and 3 of the 8 Class IIs. See Table 4 for details about the Class I and Class II YSOs.

### 3.2. The near-infrared view

Figure 1 shows a color-composed image from broadband filters J (blue), H (green), and a narrow-band filter centred on the  $2.122 \mu\text{m}$   $\text{H}_2$  line (red) of the  $4' \times 4'$  region around IRAS 00267+6611 obtained with the NOTCam WF camera. Because of the very red and bright source in the centre of the field, only very short exposures were obtained to avoid saturation of the detector. The 2MASS sources in this region are shown in a  $J - H/H - K_S$  diagramme in Fig. 3. The loci of unreddened main-sequence stars, giants and supergiants are indicated with a solid (violet), a dotted (red), and a dash-dot (blue) curve, respectively, based on their intrinsic near-IR colours tabulated in the compilation of Tokunaga (2000). We have adopted the near-IR extinction law  $A_\lambda \propto \lambda^{-2.07}$  recommended by Wang & Chen (2019) to be the best average global extinction law in the wavelength range 1 -  $3.3 \mu\text{m}$ . This gives a reddening slope in the  $J - H/H - K_S$  diagramme for the 2MASS filters of 2.0, which is depicted with a dashed line that shows the reddening vector of an A0 star. We note that for highly reddened objects the extinction law follows a curve in this diagram (Kaas 1999),

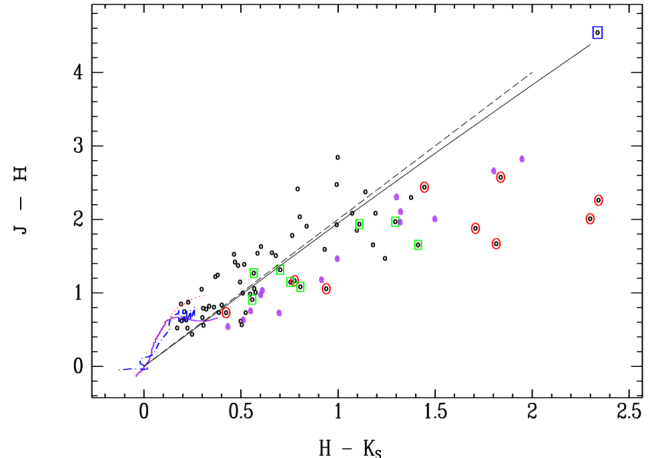


FIG. 3.— Near-IR  $J - H/H - K_S$  diagram of 2MASS sources (black circles) where the previously classified Class Is (red) and Class IIs (green) from WISE colours are marked. Additional near-IR photometry from NOTCam WF and the two HR fields that give near-IR excess are added (violet dots). For reference, the very bright and red source in Fig. 1, is indicated with a blue square and discussed in Sect. 4.4. The loci of unreddened main-sequence stars, giants and supergiants are indicated with a solid (violet), a dotted (red), and a dash-dot (blue) curve. The dashed black line shows the reddening slope of an A0 star, and the full-drawn line shows the reddening curve (see text).

as shown by the full-drawn line, where deviations away from the slope is given for the 2MASS colours by Stead & Hoare (2009). One particular object in this diagram is sufficiently reddened that this deviation is not insignificant. This is the source marked by a blue square, the very brightest object in the  $K_S$  band, see description in Sect 4.4. The previously classified YSOs from the WISE data are high-lighted in this diagramme with red circles (Class Is) and green squares (Class IIs). These sources are listed in Table 4.

To further explore the YSO content in the region we use the  $J - H/H - K_S$  diagramme to search for near-IR excess. Bona-fide near-IR excess sources are defined as those that are displaced to the right and below the reddening vector by more than  $2\sigma$  the errors in the colour indices. We find 2MASS near-IR excesses in 6 of the previously classified YSOs with WISE, but only one additional near-IR excess source is found, however, and the reason for this is the lack of valid entries for the magnitude errors in all JHK<sub>S</sub> bands. Some of the sources located in the near-IR excess region therefore do not qualify as bona-fide near-IR excess sources. For these we use instead the photometry from the short exposure NOTCam WF-camera JHK<sub>S</sub> images, and in addition, we use the two smaller fields observed with the HR-camera, their locations are marked in Fig. 7 with dashed yellow and green lines and the images are shown in Fig. 8.

Due to high extinction there are very few detections in the  $J$  band compared to the  $K_S$  band, and this limits the depth to which we can search for near-IR excess sources. Many of the sources with a large  $H - K_S$  colour index, but no detectable  $J$ -band fluxes, could be fainter YSOs embedded in the cloud, and some are already found to be Class Is using WISE, but deeper  $J$ -band photometry is needed to reliably distinguish between near-IR excess and reddened background objects. Point source fluxes



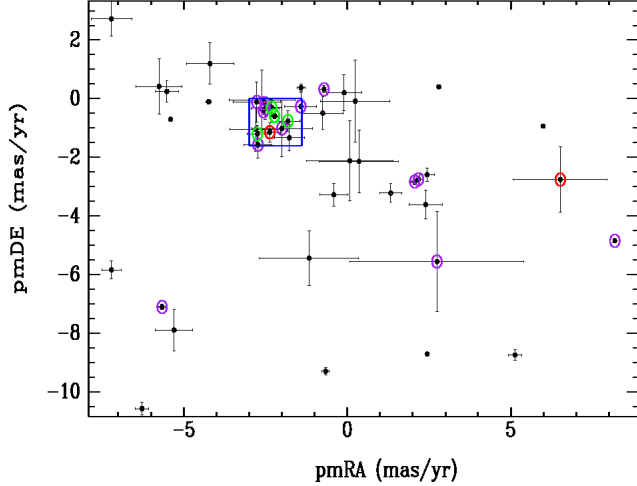


Fig. 4.— Proper motions of the 57 Gaia DR3 detected stars within the  $4' \times 4'$  region of our study (black dots with errorbars). The YSO candidates detected are colour coded as follows: red for the single Class I source, green for 4 Class II sources and violet for 13 near-IR excess or variability candidates. Most YSO candidates cluster in the blue box.

are measured to an accuracy of 10% or better down to  $J=19.4$  mag,  $H=18.2$  mag and  $K_S=14.7$  mag in the WF-camera large field and down to  $J=20.0$  mag,  $H=19.7$  mag, and  $K_S=18.7$  mag in the HR small fields, but because of uneven coverage we estimate the overall completeness to be that of 2MASS at  $J=16$  mag,  $H=15$  mag, and  $K_S=14.7$  mag. For the NOTCam sample we apply a similar criterion for near-IR excess as above, but we use a less steep reddening slope of 1.7 for the  $J-H/H-K_S$  diagramme, calculated for the NOTCam filters using the same extinction law (Wang & Chen 2019). The NOTCam photometry detects near-IR excesses in several of the previously found Class I and Class II sources and reveals 14 additional sources that we suggest as YSO candidates based on excess emission at  $2 \mu\text{m}$ . These are tabulated in Table 5, and we have added them as violet dots to the 2MASS  $J-H/H-K_S$  diagramme in Fig. 3, and note that some of them occupy the same locus as Class I sources.

When comparing the photometry obtained with 2MASS and NOTCam some stars stand out as clearly variable. Adding the magnitude errors in each band from 2MASS and NOTCam in quadrature, sources that have deviations larger than  $3\sigma$  are flagged as variable. Among 74 common sources 20 had varied by more than  $3\sigma$  in one of the bands, while 8 sources have varied in two or more bands. Among the variables are 3 Class Is, 3 Class IIs and 5 near-IR excess sources.

Using variability as a YSO criterion is tempting, as young stars are prone to vary, but some of the variations we see could be related to the different spatial resolution of the samples causing blending. In order to weed out false positives we tested the YSO candidates against Gaia (Gaia Collaboration et al. 2016) proper motions. The Gaia DR3 catalogue (Gaia Collaboration et al. 2023) lists 57 sources in the  $4' \times 4'$  area of our study. Many YSO candidates are not detected due to being embedded or highly extinguished, but proper motions were found for 2 of the Class Is, 5 of the Class IIs and 13 of the sources selected on the basis of near-IR excess or variabil-

ity. Figure 4 shows the proper motion distribution of all Gaia sources in the region (black dots with error bars), whereas the YSO candidates are encircled with colour codes. Most of the YSOs cluster around similar proper motions outlined by the blue box. The box area has been defined by the individual error bars of one Class I and 5 Class II sources, and inside the box we find 16 sources. Their median proper motions are  $-2.4 \text{ mas yr}^{-1}$  and  $-0.6 \text{ mas yr}^{-1}$ , for pmRA and pmDE, respectively. The scatter in the proper motions of these sources is 0.41 and  $0.48 \text{ mas yr}^{-1}$  in pmRA and pmDE, respectively, which is of the same order as the individual Gaia measurement errors, the mean error being  $0.43 \text{ mas yr}^{-1}$ . Thus, we cannot use the proper motion scatter to extract a YSO velocity dispersion. The intrinsic velocity dispersion is smaller than resolvable by Gaia at this distance, but we can use  $0.4 \text{ mas yr}^{-1}$  as an upper limit ( $2 \text{ km s}^{-1}$  at  $d = 1100 \text{ pc}$ ).

Regarding the variability criterion, we find that 6 variable candidates have deviating proper motions and are discarded, leaving 7 variability selected YSOs of which four are not detected by Gaia. We add these to the near-IR excess sources, giving a total of 21 YSO candidates from near-IR photometry, see Table 5. Surprisingly, one Class I source has a deviating proper motion. We note that this is the faintest of all the Class Is at  $22 \mu\text{m}$  and it is situated outside the Scuba cores (cf. Fig. 7). All the YSOs with Gaia measurements have large errors in their parallaxes, except for two of the Class IIs we use to estimate the distance (cf. Sect. 4.1).

A machine learning method to identify YSO candidates from Gaia DR2 and the AllWISE catalogue (Marton et al. 2019) finds a total of 17 candidates in the field we study. Only 6 of these co-incide with our YSO candidates, all of which have a YSO probability  $> 0.95$  in their catalogue. Three of them are the same Class IIs as found in Marton et al. (2016) and mentioned in Sect. 3.1, and two more Class IIs are recovered, and in addition one of the YSOs we classify through near-IR variability. The remaining 11 sources do not fulfill our criteria, and only three of these have  $> 90\%$  YSO probability in their study.

The final sample of YSOs in the region is shown in Fig. 7 overlaid on a submm map from Scuba/JCMT at  $850 \mu\text{m}$ , showing the dense cores in the region. The Class I protostar positions are marked with large red circles, Class II sources with green squares, near-IR excess sources with orange squares and variable sources with cyan diamonds.

### 3.3. Millimetre emission

Figure 5 shows the  $^{12}\text{CO}(1-0)$ , the  $^{13}\text{CO}(1-0)$ , and the CS(2-1) spectra taken towards IRAS 00267+6511 ((0,0) position of the map). The spectra all peak at about  $-17.0 \text{ km s}^{-1}$ , a value that can be adopted as the velocity of the gas component associated with the young stellar sources, and are consistent with the global radial velocity of PGCC G120.67+02.66 quoted by Zhang et al. (2016) in their CO survey of Planck cold cores in the second Galactic quadrant. They have mapped this region, with HPBW of about  $52''$ , using the on-the-fly (OTF) observing mode, with a scan speed of  $20'' \text{ sec}^{-1}$ , and detected strong CO emission. The CO lines were found at  $V_{LSR} = -17.56$ , with velocity resolution of  $0.17 \text{ km s}^{-1}$ .

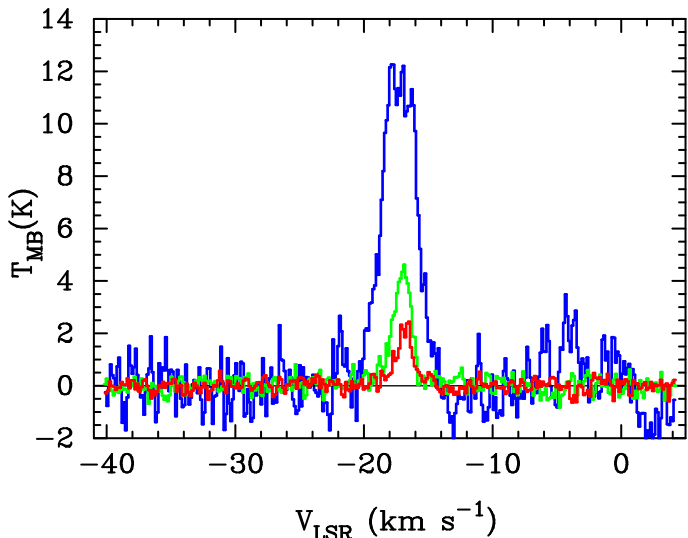


FIG. 5.— Spectra of the three observed molecular transitions towards the IRAS source ((0,0) position of the maps):  $^{12}\text{CO}(1-0)$  (blue),  $^{13}\text{CO}(1-0)$  (green), CS(2-1) (red).

HCO+ and HCN emission have also been detected (Yuan et al. 2016). Our detection of CS emission confirms the presence of high volume density gas in this region.

### 3.3.1. CO and CS emission

The  $^{12}\text{CO}(1-0)$  maps (both intensity and integrated intensity, not shown) reveal no remarkable features apart from strong emission with little spatial variation. However, the values of  $^{12}\text{CO}(1-0)$  emission, even though it is usually optically thick, can be used to derive a first estimate of the optical visual extinction  $A_V$  in the lines-of-sight of the  $^{12}\text{CO}(1-0)$  beams. This estimate is based on the empirical correlation between the  $^{12}\text{CO}(1-0)$  integrated intensity and the  $\text{H}_2$  column density along the line of sight,  $N_{i,j}$ , at position  $(i,j)$ :

$$N_{i,j}(\text{H}_2) = X \int T_{\text{MB}} dv \quad (\text{cm}^{-2}), \quad (1)$$

together with the relation  $N(\text{H}_2)/A_V = 9.4 \times 10^{20} \text{ cm}^{-2} \text{ mag}^{-1}$  (Frerking et al. 1982).

The constant  $X$  has been determined empirically by various works. Adopting the value used by May et al. (1997) for the outer Galaxy, of  $X = 3.8 \times 10^{20} \text{ cm}^{-2} (\text{K km s}^{-1})^{-1}$ , we obtain a first estimate of  $A_V = 20 \text{ mag}$ .

Figure 6 presents the contour maps of  $^{13}\text{CO}(1-0)$  integrated intensity and CS(2-1) intensity (black lines) towards IRAS 00267+6511 superimposed on  $4' \times 4'$  NOTCam  $H$ -band images. Both transitions peak about 0.7 arcmin southwest of the IRAS source revealing the presence of a molecular cloud core with high column densities and high volume densities in this region. This core is part of the source named PGCC G120.67+02.66 and mapped in  $^{12}\text{CO}$  and  $^{13}\text{CO}$  by Zhang et al. (2016), here mapped with higher angular resolution.

Around the peak of  $^{13}\text{CO}$  emission, there is a relatively slow decrease, with an extended plateau of emission (second highest contour level) where column densities remain high. The bright reddened star lies at a position within this plateau. Using the value of the  $^{13}\text{CO}$  emission, under

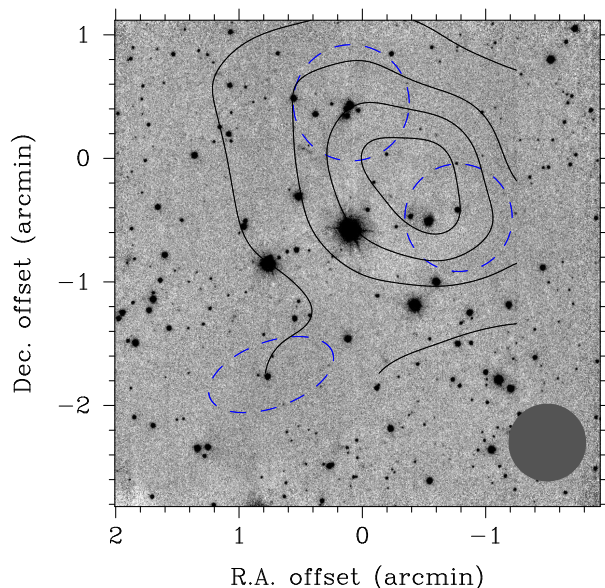
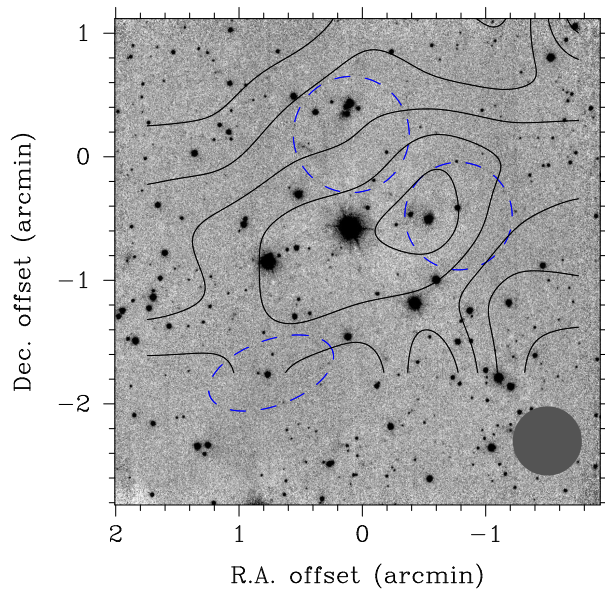


FIG. 6.— Smoothed contour maps of millimetre emission towards IRAS 00267+6511 superimposed on the NOTCam  $H$ -band image: (top)  $^{13}\text{CO}(1-0)$  integrated intensity: the lowest contour is at  $6 \text{ K km s}^{-1}$ , subsequent contours are in steps of  $0.8 \text{ K km s}^{-1}$ ; (bottom): CS(2-1) intensity: the lowest contour is at  $1.0 \text{ K}$ , subsequent contours are in steps of  $0.4 \text{ K}$ . The offsets are relative to the position of the IRAS source. The solid circle represents the telescope main beam. Notice the presence of a high column density peak and plateau on the  $^{13}\text{CO}$  map, and a high volume density core on the CS map, both about  $0'.7$  southwest of the IRAS source. The blue dashed contours represent the approximate locations and extents of the three brightest SCUBA-2 cores detected towards this region (see later in the text).

the assumptions of optically thin and LTE conditions, we derive a value of  $A_V = 6 \text{ mag}$  at the position of this star. This is clearly a lower limit, because in regions of high extinction the  $^{13}\text{CO}(1-0)$  transition is not optically thin and the calibration methods (e.g. Frerking et al. 1982), that were derived for small values of  $A_V$ , do not lead to accurate results when applied in the presence of large values of visual extinction.

The CS intensity map displays a single strong peak of

TABLE 1  
SCUBA-2 CORES IN THE REGION AROUND IRAS 00267+6511.

Number	Name	$\Delta$ R.A. (arcmin)	$\Delta$ Dec (arcmin)	Effective radius (arcmin)	Integrated flux (Jy)	Core mass ( $M_{\odot}$ )	SCOPE name Eden et al. (2019)
1	G120.652+2.681	-0.78	-0.48	0.44	2.31 (0.23)	140 (14)	G120.65+2.68
2	G120.668+2.691	0.02	0.45	0.47	2.15 (0.20)	130 (13)	G120.67+2.69
3	G120.676+2.658	0.74	-1.75	0.37	1.57 (0.16)	96 (10)	G120.68+2.66
4	G120.655+2.645	-0.45	-2.62	0.20	0.38 (0.04)	23 (2.0)	...
5	G120.689+2.678	1.42	-0.48	0.11	0.16 (0.01)	9.7 (1.0)	...

emission at approximately the same map position as the peak on the  $^{13}\text{CO}$  map. However, unlike  $^{13}\text{CO}(1-0)$ , away from the CS peak the emission exhibits a strong gradient in all directions around an elongated, approximately elliptical core with major axis oriented close to the NE–SW direction. Furthermore, a linear fit to the radial CS integrated intensity results in a radial density profile vary according to  $r^{-0.6}$ , where  $r$  is the distance to the peak intensity. Assuming optically thin emission, the column density profile has the same radial dependence. Disregarding any effects of finite cloud radius (or core edge proximity) (Yun & Clemens 1991), this implies a volum density radial profile  $n(r) \propto r^{-1.6}$ , close to  $n(r) \propto r^{-3/2}$ , the theoretical radial dependence of an infinite isothermal sphere in free-fall collapse (Shu 1977).

The YSOs identified on the infrared images lie in regions of the  $^{13}\text{CO}$  and CS maps around the plateau and the peak of maximum emission. Class II sources appear more scattered, whereas most Class I sources are located closer to the peaks of emission (see also Fig. 7), in regions of higher density, supporting their classification as Class I objects (more embedded than those classified as Class II).

### 3.3.2. Planck Galactic Cold Clumps and SCUBA-2 cores

Analysis and photometry of the 850  $\mu\text{m}$  SCUBA-2 image resulted in the identification of five sub-mm sources in the region covered by our near-infrared NOTCam images. They are listed in Table 1 (positions relative to IRAS 00267+6511, effective sizes, and 850  $\mu\text{m}$  fluxes).

The three brightest and more extended sources are also marked by blue dashed lines on Fig. 6. They coincide with three listed SCOPE cores (Eden et al. 2019) as indicated in the last column of Table 1, and were also detected by the Herschel satellite at 250, 350, and 500  $\mu\text{m}$ , where the first two brightest are seen as bright sources at all three wavelengths, and the third source is much fainter. In addition, the large scale Herschel images reveal that these cores are part of a filamentary structure that include filaments that cross at the location of these cores (hub filaments).

The two brightest SCUBA-2 cores have positions on each side of the peak of the CS map along the major axis of the elliptical CS core (Fig. 6). The brightest core (#1 in Table 1), also appears to be the densest: its location coincides with the reddest WISE source, and with the peaks of the  $^{13}\text{CO}$  and CS integrated intensity maps. Furthermore, it is the region where the CO and CS spectral lines exhibit larger line widths. Core #2 coincides with the IRAS position. The two brightest SCUBA cores roughly cover the NOTCam HR fields N and NW, respectively, seen in Fig 7.

Because dust continuum emission at sub-mm wavelengths is optically thin, we can estimate the masses of the SCUBA-2 cores. Under the assumption of constant dust temperature, the dust mass can be obtained using:

$$M_{\text{dust}} = \frac{S_{\lambda}}{\kappa_{\lambda} B_{\lambda}(T_d)} D^2$$

where  $S_{\lambda}$  is the 850  $\mu\text{m}$  flux,  $T_d$  is the dust temperature ( $T_d = 12.6$  K, Planck Collaboration et al. (2016)), and  $\kappa$  is the mass absorption coefficient (or emissivity) of the dust. We adopted a distance of 1.1 kpc (See Sect. 4.1), a dust-to-gas ratio of 1%, and a spectral index  $\beta = 2$  for the emissivity law  $\kappa_{\lambda} \propto \lambda^{-\beta}$ , with  $\kappa_{1\text{mm}} = 0.3 \text{ cm}^2 \text{ g}^{-1}$ . The derived masses of the SCUBA-2 cores are given in the last column of Table 1.

### 3.3.3. CO and CS parameters of the SCUBA-2 cores

Table 2 lists the CO and CS line parameters of each of the SCUBA-2 cores that lies within the CO or CS maps. The values listed are those of the CO or CS beams closest to the centres of each core.

TABLE 2  
CO AND CS PARAMETERS OF THE SCUBA-2 CORES.

		Core number		
		1	2	5
CO	$T_R$ (K)	11.4	11.4	...
	$\int T_R dv$ (K km s $^{-1}$ )	43.0	35.3	...
	$v_{\text{LSR}}$ (km s $^{-1}$ )	-18.11	-17.12	...
	$\Delta v$ (km s $^{-1}$ )	3.53	2.92	...
$^{13}\text{CO}$	$T_R$ (K)	3.6	4.6	4.5
	$\int T_R dv$ (K km s $^{-1}$ )	7.7	7.3	7.2
	$v_{\text{LSR}}$ (km s $^{-1}$ )	-18.30	-16.89	-17.23
	$\Delta v$ (km s $^{-1}$ )	1.99	1.49	1.51
CS	$T_R$ (K)	1.57	1.58	...
	$\int T_R dv$ (K km s $^{-1}$ )	4.2	1.96	...
	$v_{\text{LSR}}$ (km s $^{-1}$ )	-18.32	-16.55	...
	$\Delta v$ (km s $^{-1}$ )	2.52	1.17	...

## 4. DISCUSSION

### 4.1. Distance

From the spectral lines, we derive the kinematic heliocentric distance, using the peak radial velocity. This can be done using different methods namely, e.g. applying the circular rotation model by Brand & Blitz (1993), or using the Reid et al. (2014) rotation curve with the

Reid et al. (2019) updated Solar motion parameters, possibly including Monte Carlo methods (e.g. Wenger et al. 2018), among others. Using the conventional solar motion parameters, and with  $V_{\text{LSR}} = -17 \text{ km}^{-1}$ , a distance of 1.5 kpc is obtained, not far from the value of 1.75 kpc derived by Zhang et al. (2016) using the Sofue (2011) method. Zhang et al. (2018) using a Bayesian calculation derive a distance of  $0.90 \pm 0.29 \text{ kpc}$  to G120.67+02.66. However, if we adopt the Reid et al. (2014) rotation curve together with the revised values of the Galactic constants  $R_0$  and  $\Theta_0$  of Reid et al. (2019), we derive distances between 0.95 and 1.25 kpc. Interestingly, Guo et al. (2020) use data from extinction catalogues and parallaxes from Gaia DR2, together with modelling, and derive distances to Planck Galactic cold cores. They obtained a distance of  $1063 \pm 104 \text{ pc}$  to PLCKECC G120.67+02.66. Furthermore, we find that among the 8 Class II sources found in Sect. 3.1, as many as 5 have measured parallaxes in the GAIA DR3 catalogue (Gaia Collaboration et al. 2023), and two of these have relatively small errors. These two optically visible Class IIs are located relatively close to the center of the region, and we use their parallaxes at  $0.867 \pm 0.025 \text{ mas}$  and  $0.948 \pm 0.097 \text{ mas}$  to estimate a distance of  $1.1 \pm 0.05 \text{ kpc}$ . We conclude that the currently best estimate for the distance to this star formation region and molecular cloud core is 1.1 kpc.

#### 4.2. The embedded YSO population

The results from exploring the stellar population with mid-IR WISE and near-IR 2MASS and NOTCam photometry as explained in Sect. 3.1 and Sect. 3.2 demonstrate a rich collection of young stars with 9 Class I sources, 8 Class II sources, and 21 YSO candidates from the near-IR study. The total sample of 38 YSOs is shown in Fig. 7 overlaid on the  $4' \times 4'$  narrow-band  $2.122 \mu\text{m}$   $\text{H}_2$  image which for a distance of 1.1 kpc corresponds to an area of  $1.3 \text{ pc} \times 1.3 \text{ pc}$ , giving an average stellar surface density of  $24 \text{ YSOs pc}^{-2}$ . This would meet the criterion of a stellar cluster as defined in Lada & Lada (2003), who define it as a group of 35 or more physically related stars whose stellar mass density exceeds  $1.0 M_{\odot} \text{ pc}^{-3}$ .

The contours in the left panel of Fig. 7 show the high spatial resolution  $850 \mu\text{m}$  mapping from Scuba/JCMT that outlines the dense cores listed in Table 1. We note that all cores are populated with YSOs, and that most Class Is are embedded in a core. Even the two smallest cores have a Class I source inside the density contours. While the spatial distribution of the YSOs in general is relatively scattered, the Class I sources are essentially located in the cores and the remaining YSOs partly in the submm cores and partly outside.

The number ratio Class I/Class II is a measure of activity and youth since the average lifetime of the Class I stage is estimated to 0.4 Myr (Evans et al. 2009) and the duration of the Class II phase is typically taken to be 2-3 Myr (see also Dunham et al. 2015). This means that a number ratio around unity suggests the region is extremely young with on-going formation of protostars. Such high ratios are typical in environments of tight stellar groups according to the *Spitzer* based study of the solar neighbourhood (Evans et al. 2009). Gutermuth et al. (2009) finds a median Class I/Class II ratio of 0.27 in 36 star-forming cores within 1 kpc of the Sun. The 21 YSO candidates from the near-IR study cannot be clas-

sified as bona-fide Class IIs, but most are likely pre-main sequence disk sources, although Fig. 3 shows that some have very red  $H - K_S$  indices and occupy the region of Class Is, and these are too faint and/or not resolved in the WISE sample. If we would consider to add these 21 sources to the Class II category, we would obtain a lower limit number fraction of 9/29 over the whole field, which is still high.

Another indication of youth is the location of the YSOs with respect to their birthplaces, presumably in the cores. Stellar velocity dispersions obtained from radial velocity measurements in clusters with massive stars give values as high as  $3.5 \text{ km s}^{-1}$  for NGC 2264 (Fűrész et al. 2006) and  $3.3 \text{ km s}^{-1}$  for Berkeley 59 (Gahm et al. 2022), while based on Gaia DR2 Kuhn et al. (2019) find lower dispersions for these same clusters and typical values of 1-3  $\text{km s}^{-1}$  for clusters in general. In Sect. 3.2 Gaia proper motions give us an upper limit of  $2 \text{ km s}^{-1}$ . For embedded clusters, near-IR radial velocity studies find velocity dispersions of  $0.9 \text{ km s}^{-1}$  for NGC 1333 (Foster et al. 2015), a cluster which is similar to this region in many aspects; it forms low-mass stars, is embedded and young enough to contain both dense cores and protostars. With such velocities the YSOs would disperse by 0.9 pc in the time span of 1 Myr, i.e. they would escape the dense cores in less than 0.5 Myr. These considerations suggest that the age of this star formation region is likely below 1 Myr.

Given the embeddedness and the very early stage of star formation, we have not attempted to determine the masses of the YSOs.

The SCUBA-2 core #2 in Table 1 (G120.668+2.691, the northern-most in Fig 7) contains 8 identified YSOs, including two bona-fide Class I protostars, and is the core richest in detected YSOs. For a 1.1 kpc distance the effective core radius is 0.15 pc, giving a stellar surface density of  $113 \text{ YSOs pc}^{-2}$  ( $\pm 10\%$ ), which is similar to that of the central cluster (A) in the Serpens Cloud Core measured within an edge of  $A_V = 20 \text{ mag}$  (See Harvey et al. 2007, Table 6, adjusted to  $d=415 \text{ pc}$ ). Assuming symmetry in the radial direction, the volume density in this core is  $570 \text{ YSOs pc}^{-3}$ . This fits well with the definition of a tight stellar group ( $> 25 M_{\odot} \text{ pc}^{-3}$ ) by Evans et al. (2009) even if we would assign a low average stellar mass. If we assume that the mean YSO mass is  $1 M_{\odot}$  and use the estimated core mass in Table 1, the present star formation efficiency (SFE) in this core reaches  $\sim 6\%$ .

#### 4.3. Extended emission in the dense cores

Figure 7 b) shows the continuum-subtracted emission in the  $\text{H}_2 \text{ v}=1-0 \text{ S}(1)$  line at  $2.122 \mu\text{m}$ . This line is a good tracer of shock-excited emission in low-velocity shocks, and frequently used to study embedded Herbig Haro flows and protostellar jets from ground-based observations (e.g. Reipurth & Bally 2001, and references therein). The figure indicates several flows in the area of our study, at least three major flows, as well as a number of more isolated emission features. The driving sources of such embedded flows are typically found to be protostars. Velocity information of the jet structures is required to properly designate the origin of the jets, but we can by morphology and proximity relate Class I sources or near-IR excess YSOs to most of the structures, as discussed in the following.



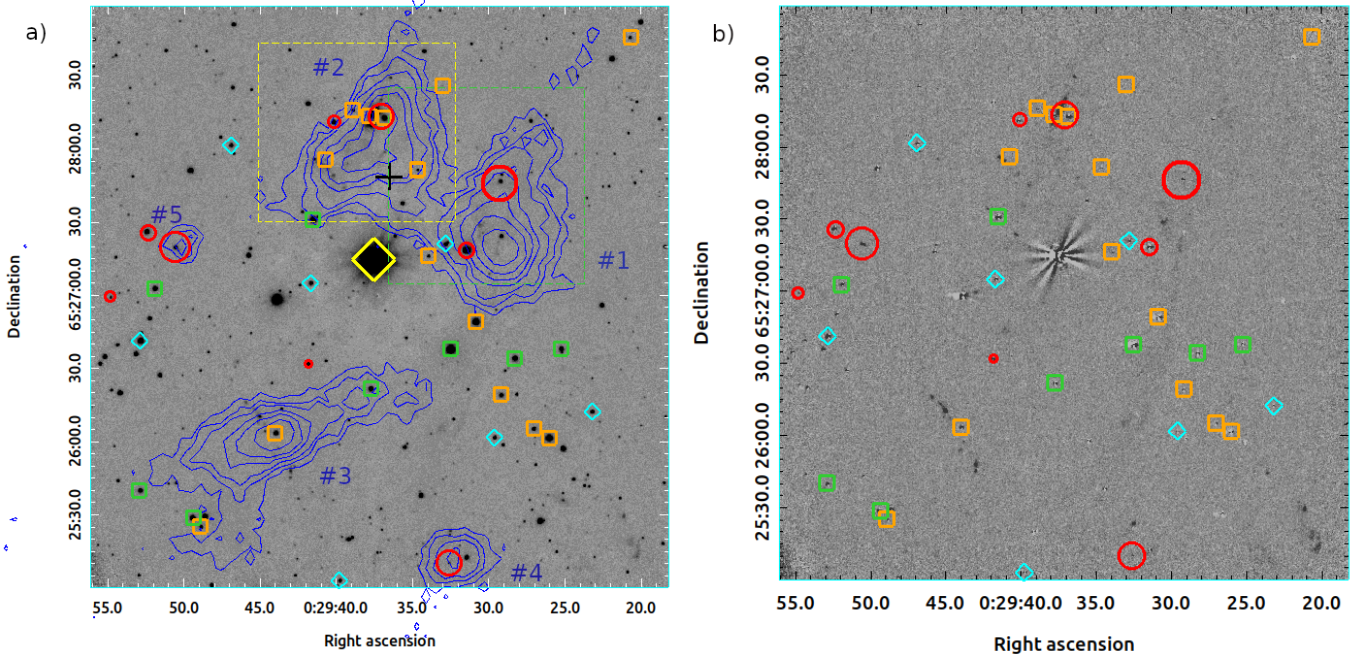


FIG. 7.— a) The YSO sample is overlaid on the  $H_2$  ( $2.122\mu\text{m}$ ) narrow-band image with the position of IRAS 00267+6511 marked (black plus sign). The SCUBA-2 cores are numbered as in Table 1, and blue contours show  $850\mu\text{m}$  continuum emission in steps of 0.2, 0.3, 0.4, 0.6, 0.8, 1.1 and  $1.6\text{ mJy per square arcsec}$ . Positions of YSOs are marked for Class I sources (red circles, where size suggests relative brightness at  $22\mu\text{m}$ ), Class II sources (green squares), near-IR excess sources (orange squares) and variable sources (cyan diamonds). The putative background supergiant (yellow diamond). The dashed boxes outline the small regions shown in Fig. 8 at higher resolution. b) Continuum subtracted  $H_2$  ( $2.122\mu\text{m}$ ) image with YSO positions marked as in panel a). Some artefacts are due to stellar PSFs not well subtracted. (Note also the diffraction spikes from the telescope spider at the bright star as the telescope field rotator adjusts.)

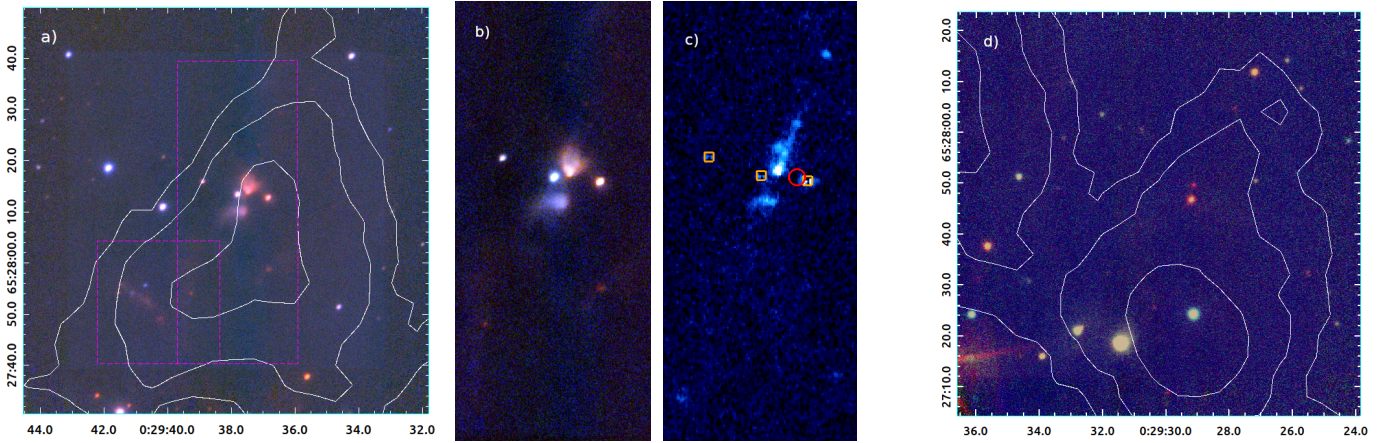


FIG. 8.— a) and d) shows NOTCam J (blue), H (green) and  $K_S$  (red) RGB images of the two smaller fields *N* and *NW*, both  $80'' \times 80''$  ( $0.43 \times 0.43\text{ pc}$ ) wide. The  $850\mu\text{m}$  emission defining the submm cores is shown (white contours) in steps of 0.2, 0.4, and  $1.0\text{ mJy per square arcsec}$ . The rectangle marked in a) is the hour-glass shaped nebulosity shown in JHKs colours in b) and with a collimated jet emerging in the  $H_2$  image in c). The tabulated position of the WISE Class I source (red circle) and three near-IR excess sources (orange squares) are marked in c).

#### 4.3.1. SCUBA-2 core G120.668+2.691 (#2)

SCUBA-2 core G120.668+2.691 (#2 in Table 1) is imaged at high-resolution in the near-IR in Fig. 8 a). This core contains a nebulosity with emission extending out from a dark center forming an hour-glass shaped nebula, which is seen in our images to extend over at least  $7''$  across the sky, corresponding to  $\sim 8000\text{ au}$ . The structure is seen in all three JHK<sub>S</sub> filters, is strongest in the  $K_S$  band, and reddest in the northern part. Such a morphology can be interpreted as scattered light from cavities formed as a bipolar jet/wind/outflow from a protostar has begun to clear the dust cocoon in the polar re-

gions. Although at a lower spatial resolution, this object looks remarkably similar to the nearby Class 0 protostar L1527 IRS as imaged by NIRCam at the James Webb Space Telescope (See Fig.1 in Tobin & Sheehan 2024). The inner region of the northern cone has a sharp peak which is, however, not a point source as it is slightly more extended ( $\text{fwhm} = 0.7''$ ) than the stellar PSF ( $\text{fwhm} = 0.4''$ ). As shown in Fig. 8 b) and c) this intensity peak in the  $K_S$  image is mainly due to a bright knot of  $H_2$  emission, and a clear distinction is seen between the cone morphology in broad band JHK<sub>S</sub> images and a narrow bipolar jet, with knots extending over a large distance,

traced by the H<sub>2</sub> line emission. In panel c) the position of the Class I source J002937.06+652813.1 from the WISE catalog is marked. It is offset from the near-IR source next to it; the 2MASS cross-correlation measure gives an offset of 1.45'' together with an extended source flag of 5, which means it falls within 5'' of an extended 2MASS source. Taking into account the WISE spatial resolution of 6'' and the high YSO density, the Class I source is likely the driving source giving rise to the nebula and the jet, having its catalog coordinates confused with the 2MASS extended source and the near-IR excess YSO to the west, which, however, could also be a Class I, judging from its location in the  $J - H/H - K$  diagramme. The jet is clearly bipolar with a northern extent of at least 20'', limited by coverage, and a southern arm of  $\sim 50''$ , judging from the furthest aligned knot, corresponding to about 0.27 pc. If we assume a typical average velocity of protostellar jet knots to be 50-100 km s<sup>-1</sup>, as found in a multi-epoch proper-motion study in Serpens (Djupvik et al. 2016), the dynamical age of this jet would be a few 10<sup>3</sup> yr.

Further to the South in field *N* several features of faint and red extended emission are seen. One particular structure is an NE/SW elongated nebulosity that looks like parts of a jet, but what could be its originating source is not obvious, see Fig.9. We found one YSO nearby from near-IR excess, and two additional red point sources could be deeply embedded YSOs, but failed to meet the classification criteria.

#### 4.3.2. SCUBA-2 core G120.652+2.681 (#1)

Most of SCUBA-2 core G120.652+2.681 (#1 in Table 1) is covered by field *NW* and shown in Fig. 8 d). This is a very dense region and we detect only 4 YSOs (cf. Fig. 7), but it includes the brightest 22  $\mu$ m source, a Class I protostar (WISE J002929.28+652746.0) that is deeply embedded and has an equally red but fainter neighbour. We note a curved tail of faint H<sub>2</sub> emission extending from this Class I position towards the south. Another Class I in this core is located in a group of YSOs in the lower part of the image in Fig. 8 d) and has some extended emission. The star located near the peak of the dense submm core is a foreground object.

#### 4.3.3. SCUBA-2 core G120.676+2.658 (#3)

The southern of the three largest SCUBA-2 cores (#3, G120.676+2.658), is more elongated and Fig. 7 a) shows that five YSOs are related to it, none of them bona-fide Class I sources. From the continuum-subtracted narrow-band 2.122  $\mu$ m H<sub>2</sub> line emission image in Fig. 7 b) we see a jet-like structure of several knots extending out from the near-IR excess source 2MASS 00294396+6526034, see Table 5, likely the driving source of this jet.

#### 4.3.4. The two smallest SCUBA-2 cores (#4 and #5)

Figure 7 a) shows that the two smaller submm cores also host Class I protostars. Towards core #4 in Table 1 the Class I source WISE J002932.58+652510.0 is located, and a knot of H<sub>2</sub> emission is found  $\sim 13''$  to the North of it. Similarly, the Class I star WISE J002941.83+652631.9, which we flag in Table 4 as a source with a deviating proper motion, could be related

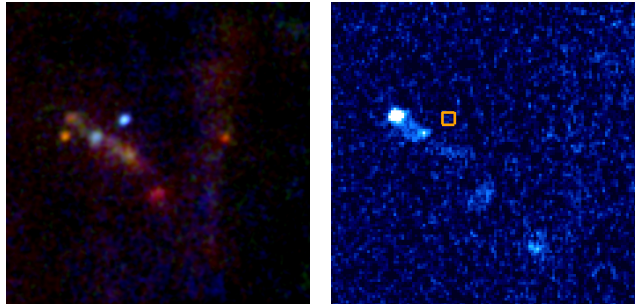


FIG. 9.— Enhancement of the jet structure in the dashed box from Fig. 8 a), and comparison between JHK<sub>S</sub> RGB coded image (left) and continuum subtracted H<sub>2</sub> image (right). Near-IR excess YSO marked with orange square.

to an H<sub>2</sub> emission knot found to the north of it, at a projected distance of approximately 0.07 pc. Finally, the Class I source (WISE J002950.58+652719.6) is seen towards the submm core #5, and seems to possess a small jet at the very vicinity of the star.

Some structures are more difficult to interpret, such as the relatively bright features in the SW corner of the image. However, an extensive investigation of these jets is outside the scope of the paper. We note that the mere presence of such a rich collection of shocked molecular gas features, most likely caused by several protostellar jets and flows, supports our conclusion that the region is at an early evolutionary star formation phase, comparable to nearby star formation regions such as NGC 1333 (Davis et al. 2008). Traced by the mass loss through collimated jets, all the submm cores in this Planck cold clump host YSOs that have gone through recent major mass accretion activity on a similar time-scale.

#### 4.4. A red supergiant star?

The brightest source in the infrared images, both in Fig. 1 and in the WISE atlas is the source 2MASS 00293749+6527146 aka WISE J002937.50+652714.7, a hindrance for deep near-IR imaging due to its strong *K* band brightness. It is located close to the centre of the region, has an extremely red colour in the near-IR, while nothing is seen in the optical except for a marginal detection in the PanSTARRS DR1 y-band image, and it is not in the Gaia DR3 catalogue. In the near-IR colour-colour diagramme in Fig. 3 the location of the source (open blue square) is consistent with it being a highly reddened supergiant or giant. In the WISE CC diagram in Fig. 2 the source has excess emission in the [3.4] – [4.6] index but not in the [4.6] – [12] index. It also has a clear excess in a  $K_S - [3.4]/[3.4] - [4.6]$  diagram, where it occupies a locus similar to that of the Class II sources, but according to the criteria of Koenig & Leisawitz (2014) the source would be rejected as a YSO because it is too bright at 3.4  $\mu$ m, as it by their definitions would enter the locus typically occupied by AGB stars. The source was also observed by the Midcourse Space Experiment (MSX), and the A band (8.28  $\mu$ m) flux in the MSX6C point source catalogue (Egan et al. 2003) is  $0.59 \pm 0.02$  Jy which translates to  $A = 4.99$  mag using 58.49 Jy for zeroth magnitude (Egan et al. 1999).

The NOTCam photometry obtained in 2023 shows that the source has faded by about 0.2 mag in all bands



TABLE 3  
IR PHOTOMETRY OF THE RED SUPERGIANT CANDIDATE.

	$J$ (mag)	$H$ (mag)	$K_S$ (mag)	
2MASS	$13.77 \pm 0.03$	$9.23 \pm 0.03$	$6.89 \pm 0.02$	
NOTCam	$13.97 \pm 0.02$	$9.54 \pm 0.03$	$7.09 \pm 0.05$	
	[3.4] (mag)	[4.6] (mag)	[12] (mag)	[22] (mag)
WISE	$6.06 \pm 0.10$	$5.19 \pm 0.07$	$5.13 \pm 0.02$	$4.61 \pm 0.03$

since the 2MASS measurement obtained in 1999, see Table 3. The MSX A band variability flag indicates that the source has varied over the course of the MSX mission (1996-1997) by more than  $3\sigma$ . The WISE variability flag is 2 for the [3.4] and [4.6] bands, which means a small probability of being variable in the three epochs over the WISE mission.

A K-band spectrum of the source is shown in Fig. 10. Its prominent and deep CO bandhead absorptions at  $2.2935 \mu\text{m}$  ( $2-0$ ),  $2.3227 \mu\text{m}$  ( $3-1$ ), and  $2.3535 \mu\text{m}$  ( $4-2$ ) together with the absorptions of the Ca I triplet around  $2.263 \mu\text{m}$  and the Na I doublet around  $2.207 \mu\text{m}$ , and no appreciable  $\text{Br}\gamma$  at  $2.166 \mu\text{m}$ , concur to indicate a late spectral type. We measure the equivalent widths (EWs) as described in Comerón et al. (2004) and find the EWs of the Na I doublet ( $2.2062, 2.2090 \mu\text{m}$ ) to be  $5.1 \text{ \AA}$  and the Ca I triplet ( $2.2614, 2.2631, 2.2657 \mu\text{m}$ ) to be  $4.7 \text{ \AA}$ . The reference continuum was measured on both sides of the features and the errors are estimated to be  $< 1 \text{ \AA}$ . We have measured the EW of the  $2.29 \mu\text{m}$  CO ( $2-0$ ) absorption feature from  $2.2920$  to  $2.3020 \mu\text{m}$ , i.e. over wavelength range of  $0.010 \mu\text{m}$ , using reference continuum levels on the blue side of the feature extrapolated to the red side, and we find  $\text{EW}_{\text{CO}(2-0)} = 25.5 \pm 1 \text{ \AA}$ . These measured EWs are very similar to those measured for red supergiants (e.g. Comerón et al. 2004, 2016). Using the relation between spectral type and the EW of CO ( $2-0$ ) established in Davies et al. (2007), which is based on the spectral type versus temperature calibration of Levesque et al. (2005), a tentative IR spectral type of M2 I can be assigned to the target. We caveat that a later M-type giant could also reach similarly deep CO absorptions, although in that case the water steam bands are often prominent, and we do not see any notable depression shortwards of  $2.1 \mu\text{m}$  in this target. Comparison was made with the near-IR spectral atlases by Wallace & Hinkle (1997) and Lançon & Wood (2000). With help of the online archive of spectra of luminous cool stars in numerical form provided by Lançon & Wood (2000), we could measure the EW of the  $2.29 \mu\text{m}$  CO feature in the same manner as for our target for two M2 supergiants and one M5.5 giant and find that our target has an EW in between the two types.

The star’s auspicious position at the very centre of the star formation region raises the question of whether it could be an embedded outburst object. We can probably exclude that it is an FU Orionis outburst, although they present similarly deep CO absorption bands and are often bluer when in outburst (Szegedi-Elek et al. 2020), because its luminosity would be an order of magnitude larger than what is typical for FUORs, and furthermore, the Na I and Ca I absorptions in the K-band spectrum

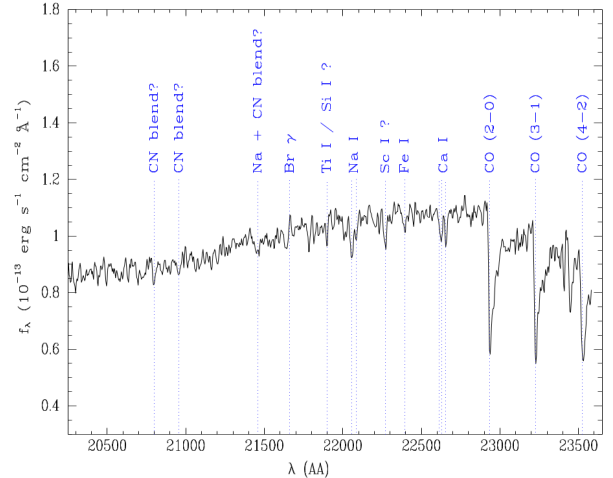


FIG. 10.— NOTCam K-band spectrum of the red luminous star showing the telltale signature of a late type star; very strong CO bandhead absorptions, as well as the Ca I triplet at  $2.263 \mu\text{m}$  and the Na I doublet at  $2.207 \mu\text{m}$  in absorption.

are too strong for such an interpretation (Connelley & Reipurth 2018).

According to Elias et al. (1985) the intrinsic  $H - K_S$  colour for the M2 I spectral type is  $(H - K_S)_0 = 0.22$  mag, while that of an M5.5 III spectral type is  $0.29$  mag (Bessell & Brett 1988, see compilation by Tokunaga (2000)). This gives quite a similar a colour excess in both cases,  $E(H - K_S) = (H - K_S)_{\text{obs}} - (H - K_S)_0$ , of  $2.12$  mag and  $2.05$  mag for M2 I and M5 III, respectively. From the Wang & Chen (2019) near-IR extinction law the relation  $A_K = 1.33 \times E(H - K_S)$  gives  $A_K = 2.82$  mag and  $2.72$  mag for M2 I and M5 III, respectively. This translates to around  $36$  magnitudes of visual extinction using  $A_K = 0.078 A_V$ , i.e. the source is extremely reddened even though its projected location is just offset from the densest submm cores, see Fig. 7. The expected absolute magnitude of an M5 giant is  $M_V = -0.3$  mag and that of an M2 supergiant is  $M_V = -5.6$  mag (Cox 2000). The respective intrinsic colours from the above references are  $V - K = 5.96$  mag and gives  $M_K = -6.3$  mag (M5 giant) and  $V - K = 4.1$  mag giving  $M_K = -9.7$  mag (M2 supergiant). We can make a rough estimate of the distances required to reach such absolute K-band magnitudes via the relation  $M_K = m_K - A_K - 5 \log d - 5$ , and we find  $1.2$  kpc and  $5.7$  kpc for the M5 giant and the M2 supergiant, respectively. Thus, we cannot use the distance argument to exclude the possibility that the source is a late M-type giant. The measured extinction requires the source to be behind the star formation region at  $1.1$  kpc. If it is a giant, however, the uncertainties in the above reasoning would put it at a distance compatible with the cloud, but owing to the advanced age of a giant, it would be unlikely that it is related to the cloud.

#### 4.5. Star formation scenario

The G120.69+2.66 cold clump, which appears to be the central hub of a larger Herschel filament, contains several dense submm cores, all of which host protostars and/or signs of on-going low-mass star formation. On the other hand, it has been suggested (Tang et al. 2018;

Yi et al. 2018; Zhang et al. 2018) that Planck cold clumps have low levels of star formation activity, while Wu et al. (2012) and Liu et al. (2013) indicated that they are more quiescent and less evolved than the typical star-forming region. The values of the radii, masses, and mass surface densities of these cores in G120.69+2.66 fit within the range of the corresponding derived values for compact sources in the recent study of Galactic Plane Planck cold clumps (Eden et al. 2024), and thus indicate that these cores are typical members of the family of compact sources identified in Galactic Plane Planck cold clumps. However, the submm cores in G120.69+2.66 have radii (0.04 to 0.15 pc) that place them at the shorter end of the distribution of sizes of the Eden et al. (2024) compact sources, and have mass surface densities that are at the higher end of the distribution of mass surface densities. This appears to indicate that G120.69+2.66 belongs to the group of more active Planck cold clumps that are currently sites with on-going star formation.

In the previous sections we argue that the star formation process must be in an early stage, and in fact Juvela et al. (2018) found that any correlation of Planck cold clumps with young stellar objects tends to be the youngest protostellar stages. Here we compare with well-studied, nearby low-mass embedded clusters that exhibit similar sub-structure and dense cores, co-existing with protostars and more evolved YSOs. Several such regions were studied by the Spitzer c2d survey (e.g. Evans et al. 2009, and references therein). An inspection of the youngest embedded clusters, NGC 1333 at a distance of 296 pc (Kuhn et al. 2019) and Serpens Main at 415 pc (Dzib et al. 2010), show many similarities with G120.69+2.66. Lada & Lada (2003) described these as the least evolved embedded clusters known and likely no more than 1 Myr of age.

The Class I sources in G120.69+2.66 are practically all seen projected on to dense submm cores. This was shown for Serpens Main (e.g. Kaas et al. 2004, Fig. 11) and is particularly well demonstrated in NGC 1333 (Gutermuth et al. 2008, Fig. 10), where the Class I sources perfectly trace the dense submm cores, giving a picture of the pristine early phase of the formation of a cluster. Counting those YSOs for which we have bona-fide mid-IR classification, the Class I/Class II number ratio in our region is similar to that of the Serpens Main core, found to be among the highest in a survey of 60 cluster cores (Gutermuth et al. 2009), and for which it has been suggested that star formation has proceeded in several phases (Casali et al. 1993; Kaas et al. 2004); the clustered protostar population having formed in a recent burst.

The apparently most active submm core has a surface density of YSOs  $\sim 100 \text{ pc}^{-2}$ , which is only slightly lower than that of both the NGC 1333 and the Serpens Main cores of  $\sim 140 \text{ pc}^{-2}$  (Gutermuth et al. 2009, adjusted to updated distances). By assuming an average stellar mass of  $1 M_{\odot}$  we estimate the current star formation efficiency (SFE) locally in this core to be about 6%. For comparison a SFE of 13-15% was found for the NGC 1333 cores (Jørgensen et al. 2008).

The large number of extended molecular hydrogen objects we find in G120.69+2.66 reminds us of those in NGC 1333 and Serpens Main, i.e. well studied outflows with protostellar jets from Class 0/I sources (Davis et al. 2008; Green et al. 2024). We can only speculate about

the origin of some of the extended molecular hydrogen objects in G120.69+2.66 that do not have an obvious driving source, whether they are protostellar jets, and also to what extent there are embedded protostars that have escaped our detection and classification.

With the limited observations currently available in this study, we are most likely just “scraping the surface” of the YSO population. In spite of that, we find striking similarities with the youngest nearby embedded clusters and envision a similar star formation scenario. Deep mid- and far-IR observations are required to further investigate this.

## 5. SUMMARY

1. The IRAS 00267+6511 region, located towards the outer Galaxy at a distance of 1.1 kpc, comprises embedded on-going star formation. Both millimetre (CO and CS) lines and  $850\mu\text{m}$  continuum emission reveal the presence of dense gas and dust in a molecular cloud containing one dense clump (PGCC G120.67+2.66) resolved into five SCUBA-2 cores.
2. Near- and mid-IR photometry is used to identify 38 YSOs with infrared excesses and/or variability, giving an average stellar surface density of  $24 \text{ YSO pc}^{-2}$  and reaching up to  $113 \text{ YSO pc}^{-2}$  in the richest populated submm core (#2), for which we estimate the star formation efficiency to be  $\sim 6\%$ .
3. We classify 9 bona-fide Class Is and 8 bona-fide Class IIs, and most of the remaining YSOs are likely to be of Class II category. The high Class I/Class II number ratio, as well as the spatial distribution of the YSOs with respect to the dense submm cloud cores, suggests that star formation is still in a very early stage. The region is likely younger than 1 Myr.
4. Narrow-band  $\text{H}_2$  line imaging at  $2.122 \mu\text{m}$  detects a number of features, jet-like structures as well as isolated knots. The morphology and proximity to protostars is used to interpret flow structure and possible originating YSOs. The number of flows suggest recent episodes of mass accretion in several of the YSOs in the region.
5. Near-IR imaging reveals in one of the dense cores an hour-glass shaped nebula, likely the result of a deeply embedded YSO carving out its dust cocoon through a bipolar outflow. The  $\text{H}_2$  images present a collimated jet emerging from inside the cone.
6. G120.69+2.66 appears to belong to the group of more active Planck cold clumps that are currently sites with on-going star formation in the youngest protostellar stages.
7. We have discovered a very bright and reddened object seen towards the centre of this star formation region. Its spectrum shows it to have a cool temperature, we assume the infrared spectral type is around M2, and it is likely a red supergiant. If so, it is located far behind the cloud in the outer



Galaxy and was previously unknown, despite its brightness, due to the very high foreground extinction in this region.

We thank two anonymous referees for thoughtful remarks.

Part of this work was supported by Fundação para a Ciência e a Tecnologia (FCT) through the research grants UIDB/04434/2020 and UIDP/04434/2020. JLY acknowledges support from Onsala Space Observatory for the provisioning of its facilities/observational support. The Onsala Space Observatory national research infrastructure is funded through Swedish Research Council grant No 2017-00648.

Partly based on observations made with the Nordic Optical Telescope, owned in collaboration by the University of Turku and Aarhus University, and operated jointly by Aarhus University, the University of Turku and the University of Oslo, representing Denmark, Finland and Norway, the University of Iceland and Stockholm University at the Observatorio del Roque de los Muchachos, La Palma, Spain, of the Instituto de Astrofísica de Canarias. We thank the NOT students Niilo Koivisto and Benjamin Nobre Hauptmann for contributing to the NOTCam observations.

This publication makes use of data products from the Wide-field Infrared Survey Explorer, which is a joint project of the University of California, Los Angeles, and the Jet Propulsion Laboratory/California Institute of Technology, funded by the National Aeronautics and Space Administration.

This publication makes use of data products from the Two Micron All Sky Survey, which is a joint project of the University of Massachusetts and the Infrared Processing and Analysis Center/California Institute of Technology, funded by the National Aeronautics and Space Administration and the National Science Foundation.

This research has made use of the SIMBAD database, operated at CDS, Strasbourg, France.

This research has made use of the VizieR catalogue access tool, CDS, Strasbourg, France (DOI : 10.26093/cds/vizier). The original description of the VizieR service was published in 2000, *A&AS* 143, 23.

This work has made use of data from the European Space Agency (ESA) mission *Gaia* (<https://www.cosmos.esa.int/gaia>), processed by the *Gaia* Data Processing and Analysis Consortium (DPAC, <https://www.cosmos.esa.int/web/gaia/dpac/consortium>). Funding for the DPAC has been provided by national institutions, in particular the institutions participating in the *Gaia* Multilateral Agreement.

#### REFERENCES

- Abbott, T. M., Aspin, C., Sorensen, A. N., et al. 2000, in Society of Photo-Optical Instrumentation Engineers (SPIE) Conference Series, Vol. 4008, Optical and IR Telescope Instrumentation and Detectors, ed. M. Iye & A. F. Moorwood, 714–719
- Adams, F. C., Lada, C. J., & Shu, F. H. 1987, *ApJ*, 312, 788
- André, P., Di Francesco, J., Ward-Thompson, D., et al. 2014, in Protostars and Planets VI, ed. H. Beuther, R. S. Klessen, C. P. Dullemond, & T. Henning, 27–51
- Andre, P., Ward-Thompson, D., & Barsony, M. 1993, *ApJ*, 406, 122
- Bessell, M. S. & Brett, J. M. 1988, *PASP*, 100, 1134
- Brand, J. & Blitz, L. 1993, *A&A*, 275, 67
- Casali, M. M., Eiroa, C., & Duncan, W. D. 1993, *A&A*, 275, 195
- Comerón, F., Djupvik, A. A., Schneider, N., & Pasquali, A. 2016, *A&A*, 586, A46
- Comerón, F., Torra, J., Chiappini, C., et al. 2004, *A&A*, 425, 489
- Connelley, M. S. & Reipurth, B. 2018, *ApJ*, 861, 145
- Cox, A. N. 2000, Allen’s astrophysical quantities
- Davies, B., Figer, D. F., Kudritzki, R.-P., et al. 2007, *ApJ*, 671, 781
- Davis, C. J., Scholz, P., Lucas, P., Smith, M. D., & Adamson, A. 2008, *MNRAS*, 387, 954
- Djupvik, A. A. & Andersen, J. 2010, in Astrophysics and Space Science Proceedings, Vol. 14, Highlights of Spanish Astrophysics V, 211
- Djupvik, A. A., Liimets, T., Zinnecker, H., et al. 2016, *A&A*, 587, A75
- Dunham, M. M., Allen, L. E., Evans, Neal J., I., et al. 2015, *ApJS*, 220, 11
- Dzib, S., Loinard, L., Mioduszewski, A. J., et al. 2010, *ApJ*, 718, 610
- Eden, D. J., Liu, T., Kim, K.-T., et al. 2019, *MNRAS*, 485, 2895
- Eden, D. J., Liu, T., Moore, T. J. T., et al. 2024, *MNRAS*, 530, 5192
- Egan, M. P., Price, S. D., Kraemer, K. E., et al. 2003, VizieR Online Data Catalog: MSX6C Infrared Point Source Catalog. The Midcourse Space Experiment Point Source Catalog Version 2.3 (October 2003), VizieR On-line Data Catalog: V/114. Originally published in: Air Force Research Laboratory Technical Report AFRL-VS-TR-2003-1589 (2003)
- Egan, M. P., Price, S. D., Moshir, M. M., Cohen, M., & Tedesco, E. 1999, The Midcourse Space Experiment Point Source Catalog Version 1.2 Explanatory Guide, Technical Report, AD-A381933; AFRL-VS-TR-1999-1522
- Elias, J. H., Frogel, J. A., & Humphreys, R. M. 1985, *ApJS*, 57, 91
- Evans, Neal J., I., Dunham, M. M., Jørgensen, J. K., et al. 2009, *ApJS*, 181, 321
- Fűrész, G., Hartmann, L. W., Szentgyorgyi, A. H., et al. 2006, *ApJ*, 648, 1090
- Foster, J. B., Cottaar, M., Covey, K. R., et al. 2015, *ApJ*, 799, 136
- Frerking, M. A., Langer, W. D., & Wilson, R. W. 1982, *ApJ*, 262, 590
- Gahm, G. F., Wilhelm, M. J. C., Persson, C. M., Djupvik, A. A., & Portegies Zwart, S. F. 2022, *A&A*, 663, A111
- Gaia Collaboration, Prusti, T., de Bruijne, J. H. J., et al. 2016, *A&A*, 595, A1
- Gaia Collaboration, Vallenari, A., Brown, A. G. A., et al. 2023, *A&A*, 674, A1
- Green, J. D., Pontoppidan, K. M., Reiter, M., et al. 2024, *ApJ*, 972, 5
- Greene, T. P., Wilking, B. A., Andre, P., Young, E. T., & Lada, C. J. 1994, *ApJ*, 434, 614
- Guo, H.-L., Chen, B.-Q., Li, G.-X., et al. 2020, *Monthly Notices of the Royal Astronomical Society*, 500, 3743
- Gutermuth, R. A., Megeath, S. T., Myers, P. C., et al. 2009, *ApJS*, 184, 18
- Gutermuth, R. A., Myers, P. C., Megeath, S. T., et al. 2008, *ApJ*, 674, 336
- Harvey, P., Merín, B., Huard, T. L., et al. 2007, *ApJ*, 663, 1149
- Holland, W. S., Bintley, D., Chapin, E. L., et al. 2013, *Monthly Notices of the Royal Astronomical Society*, 430, 2513
- Jørgensen, J. K., Johnstone, D., Kirk, H., et al. 2008, *ApJ*, 683, 822
- Juvela, M., He, J., Pattle, K., et al. 2018, *A&A*, 612, A71
- Kaas, A. A. 1999, *AJ*, 118, 558
- Kaas, A. A., Olofsson, G., Bontemps, S., et al. 2004, *A&A*, 421, 623
- Koenig, X. P. & Leisawitz, D. T. 2014, *ApJ*, 791, 131
- Kuhn, M. A., Hillenbrand, L. A., Sills, A., Feigelson, E. D., & Getman, K. V. 2019, *ApJ*, 870, 32
- Lada, C. J. & Lada, E. A. 2003, *ARA&A*, 41, 57

- Lada, C. J. & Wilking, B. A. 1984, *ApJ*, 287, 610  
 Lançon, A. & Wood, P. R. 2000, *A&AS*, 146, 217  
 Levesque, E. M., Massey, P., Olsen, K. A. G., et al. 2005, *ApJ*, 628, 973  
 Liu, T., Kim, K.-T., Juvela, M., et al. 2018, *The Astrophysical Journal Supplement Series*, 234, 28  
 Liu, T., Wu, Y., & Zhang, H. 2013, *ApJ*, 775, L2  
 Marton, G., Ábrahám, P., Szegedi-Elek, E., et al. 2019, *MNRAS*, 487, 2522  
 Marton, G., Tóth, L. V., Paladini, R., et al. 2016, *Monthly Notices of the Royal Astronomical Society*, 458, 3479  
 May, J., Alvarez, H., & Bronfman, L. 1997, *A&A*, 327, 325  
 McCaughrean, M. J., Rayner, J. T., & Zinnecker, H. 1994, *ApJ*, 436, L189  
 Palmeirim, P. M. & Yun, J. L. 2010, *A&A*, 510, A51  
 Planck Collaboration, Adam, R., Ade, P. A. R., et al. 2016, *A&A*, 594, A1  
 Planck Collaboration, Ade, P. A. R., Aghanim, N., et al. 2011, *A&A*, 536, A7  
 Reid, M. J., Menten, K. M., Brunthaler, A., et al. 2019, *ApJ*, 885, 131  
 Reid, M. J., Menten, K. M., Brunthaler, A., et al. 2014, *ApJ*, 783, 130  
 Reipurth, B. & Bally, J. 2001, *ARA&A*, 39, 403  
 Shu, F. H. 1977, *ApJ*, 214, 488  
 Skrutskie, M. F., Cutri, R. M., Stiening, R., et al. 2006, *AJ*, 131, 1163  
 Sofue, Y. 2011, *PASJ*, 63, 813  
 Stead, J. J. & Hoare, M. G. 2009, *MNRAS*, 400, 731  
 Strom, K. M., Strom, S. E., & Merrill, K. M. 1993, *ApJ*, 412, 233  
 Szegedi-Elek, E., Ábrahám, P., Wyrzykowski, L., et al. 2020, *ApJ*, 899, 130  
 Tang, M., Liu, T., Qin, S.-L., et al. 2018, *ApJ*, 856, 141  
 Tobin, J. J. & Sheehan, P. D. 2024, arXiv e-prints, arXiv:2403.15550  
 Tokunaga, A. T. 2000, in *Allen's Astrophysical Quantities*, ed. A. N. Cox, 143  
 Wallace, L. & Hinkle, K. 1997, *ApJS*, 111, 445  
 Wang, S. & Chen, X. 2019, *ApJ*, 877, 116  
 Wenger, T. V., Balsaer, D. S., Anderson, L. D., & Bania, T. M. 2018, *ApJ*, 856, 52  
 Wilson, A. J., Lakeland, B. S., Wilson, T. J., & Naylor, T. 2023, *MNRAS*, 521, 354  
 Winston, E., Hora, J. L., & Tolls, V. 2020, *AJ*, 160, 68  
 Wright, E. L., Eisenhardt, P. R. M., Mainzer, A. K., et al. 2010, *AJ*, 140, 1868  
 Wu, Y., Liu, T., Meng, F., et al. 2012, *ApJ*, 756, 76  
 Yi, H.-W., Lee, J.-E., Liu, T., et al. 2018, *ApJS*, 236, 51  
 Yuan, J., Wu, Y., Liu, T., et al. 2016, *ApJ*, 820, 37  
 Yun, J. L. & Clemens, D. P. 1991, *ApJ*, 381, 474  
 Yun, J. L., Clemens, D. P., Moreira, M. C., & Santos, N. C. 1997, *ApJ*, 479, L71  
 Yun, J. L., Elia, D., Djupvik, A. A., Torrelles, J. M., & Molinari, S. 2015, *MNRAS*, 452, 1523  
 Yun, J. L., Santos, C. A., Clemens, D. P., et al. 2001, *A&A*, 372, L33  
 Zhang, C.-P., Liu, T., Yuan, J., et al. 2018, *ApJS*, 236, 49  
 Zhang, T., Wu, Y., Liu, T., & Meng, F. 2016, *ApJS*, 224, 43

provides fast and easy peer review for new papers in the **astro-ph** section of the arXiv, making the reviewing process simpler for authors and referees alike. Learn more at <http://astro.theoj.org>.

This paper was built using the Open Journal of Astrophysics L<sup>A</sup>T<sub>E</sub>X template. The OJA is a journal which

TABLE 4  
THE 17 YSOs FOUND FROM WISE MID-IR COLOURS, LISTED TOGETHER WITH 2MASS NEAR-IR COLOURS AND ERRORS WHEN AVAILABLE. THE YSO CLASS IS GIVEN IN THE LAST COLUMN. SEE SECT. 3.1 FOR DETAILS.

WISE ID	$J - H$ mag	$\sigma_{J-H}$ mag	$H - K_S$ mag	$\sigma_{H-K_S}$ mag	[3.4] - [4.6] mag	$\sigma_{3.4-4.6}$ mag	[4.6] - [12] mag	$\sigma_{4.6-12}$ mag	[4.6] mag	$\sigma_{4.6}$ mag	Class
J002941.83+652631.9 <sup>c</sup>	1.16	0.09	0.78	0.07	1.23	0.03	2.67	0.05	11.60	0.02	I <sup>a</sup>
J002954.81+652659.2					1.92	0.08	3.72	0.04	12.26	0.03	I
J002952.30+652725.3	2.44		1.44	0.06	0.88	0.03	3.29	0.03	11.39	0.02	I
J002950.58+652719.6 <sup>c</sup>	2.01	0.15	2.30	0.08	1.89	0.03	2.90	0.02	8.42	0.02	I
J002932.58+652510.0					2.81	0.03	3.76	0.02	9.16	0.02	I
J002929.28+652746.0	2.57		1.84		2.56	0.03	3.51	0.02	8.33	0.02	I
J002931.45+652718.4	1.67		1.82	0.10	1.40	0.03	2.81	0.02	8.75	0.02	I
J002937.06+652813.1	1.88		1.71		1.62	0.03	2.12	0.02	8.18	0.02	I <sup>b</sup>
J002940.09+652811.1 <sup>c</sup>	1.06	0.12	0.94	0.09	1.27	0.03	2.62	0.03	10.73	0.02	I
J002949.31+652528.5	1.93		1.11	0.05	0.76	0.03	1.86	0.03	9.65	0.02	II
J002952.88+652539.9	1.65		1.41	0.10	0.96	0.03	1.94	0.05	11.63	0.02	II
J002951.92+652702.7 <sup>c</sup>	1.27	0.07	0.57	0.06	0.79	0.03	2.32	0.05	11.74	0.02	II
J002932.47+652637.7 <sup>c</sup>	0.91	0.04	0.56	0.04	0.65	0.03	1.80	0.03	9.07	0.02	II
J002925.19+652637.7	1.08	0.06	0.81	0.05	0.70	0.03	1.72	0.06	11.57	0.02	II
J002928.25+652634.1 <sup>c</sup>	1.31	0.05	0.70	0.05	0.57	0.04	2.00	0.05	11.39	0.02	II
J002937.69+652621.7 <sup>c</sup>	1.15	0.05	0.76	0.05	0.84	0.03	2.42	0.03	10.66	0.02	II
J002941.52+652730.9 <sup>c</sup>	1.97		1.29		1.04	0.03	1.69	0.03	9.41	0.02	II

Notes:

<sup>a</sup>Has a deviating proper motion and is located outside the dense cores.

<sup>b</sup>Candidate WISE originating source for the hour-glass shaped nebula, in which case both coordinates and 2MASS cross-correlation, here taken from the WISE catalogue, are uncertain, See Sect. 4.3.

<sup>c</sup>YSO candidate in Marton et al. (2016) and/or Marton et al. (2019).

TABLE 5  
THE 21 ADDITIONAL YSO CANDIDATES FOUND IN THE NOTCAM AND 2MASS SAMPLE, SELECTED FROM EITHER NEAR-IR EXCESS OR VARIABILITY OR BOTH. THE CROSS-CORRELATED 2MASS POINT SOURCE DETECTION IS GIVEN AS AN ID WHILE THE RA/DEC COORDINATES, AS WELL AS THE NEAR-IR MAGNITUDES AND COLOURS ARE FROM THE NOTCAM DATA.

2MASS-ID	RAJ2000 deg	DEJ2000 deg	$H$ mag	$\sigma_H$ mag	$J - H$ mag	$\sigma_{J-H}$ mag	$H - K_S$ mag	$\sigma_{H-K}$ mag	YSO criterion
00292061+6528458	7.33595	65.47936	15.85	0.03	1.18	0.05	0.92	0.16	NIR excess
00292316+6526123 <sup>a</sup>	7.34653	65.43672	14.83	0.03	1.22	0.04	0.58	0.10	Variable $H$
00292601+6526014	7.35837	65.43375	12.12	0.03	0.54	0.03	0.43	0.06	NIR excess
00292700+6526051	7.36250	65.43478	14.53	0.03	1.03	0.04	0.61	0.09	NIR excess
00292916+6526190	7.37149	65.43862	14.23	0.03	0.76	0.04	0.55	0.08	NIR excess
00292956+6526017	7.37326	65.43379	15.19	0.03	1.59	0.04	0.86	0.10	Variable $H$
00293083+6526490	7.37846	65.44699	12.72	0.03	2.31	0.04	1.30	0.06	NIR excess
00293280+6527210	7.38667	65.45583	15.25	0.03	2.26	0.05	1.02	0.10	Variable $K_S$
	7.38748	65.47388	18.80	0.06	0.73	0.08	0.70	0.09	NIR excess
00293391+6527157	7.39133	65.45448	16.59	0.04	2.66	0.08	1.80	0.06	NIR excess
	7.39428	65.46428	16.55	0.04	1.46	0.06	1.00	0.06	NIR excess
00293683+6528128	7.40348	65.47021	15.91	0.04	2.82	0.09	1.95	0.10	NIR excess
00293773+6528134	7.40753	65.47038	15.37	0.04	1.96	0.06	1.32	0.06	NIR excess
00293889+6528160	7.41210	65.47108	17.05	0.04	2.01	0.07	1.50	0.06	NIR excess
00293975+6525030	7.41569	65.41750	14.82	0.03	0.81	0.04	0.03	0.15	Variable $J + K_S$
	7.41967	65.46547	18.58	0.05	0.63	0.07	0.51	0.09	NIR excess
00294167+6527049	7.42367	65.45137	14.61	0.03	1.23	0.04	0.23	0.11	Variable $H + K_S$
00294396+6526034	7.43321	65.43431	13.95	0.03	0.97	0.04	0.60	0.08	NIR excess, bipolar $H_2$ jet
00294693+6528014	7.44546	65.46706	14.58	0.03	1.03	0.04	-0.18	0.13	Variable $K_S$
00294889+6525251	7.45369	65.42361	15.88	0.03	2.11	0.06	1.32	0.12	NIR excess, Variable $H + K_S$
00295286+6526412	7.47025	65.44478	13.43	0.03	1.96	0.04	0.80	0.07	Variable $K_S$

Notes:

<sup>a</sup>YSO candidate in Marton et al. (2019).